Bistatic-like Differential SAR Tomography

Nan Ge, Xiao Xiang Zhu, *Senior Member, IEEE*

***Abstract*—Motivated by prospective synthetic aperture radar (SAR) satellite missions, this paper addresses the problem of differential SAR tomography (D-TomoSAR) in urban areas using spaceborne bistatic or pursuit monostatic acquisitions. A bistatic or pursuit monostatic interferogram is not subject to significant temporal decorrelation or atmospheric phase screen and therefore ideal for elevation reconstruction. We propose a framework that incorporates this reconstructed elevation as deterministic prior into deformation estimation, which uses conventional repeat-pass interferograms generated from bistatic or pursuit monostatic pairs. By means of theoretical and empirical analyses, we show that this framework is, in the pursuit monostatic case, both statistically and computationally more efficient than standard D-TomoSAR. In the bistatic case, its theoretical bound is no worse by a factor of 2. We also show that reasonable results can be obtained by using merely 6 TanDEM-X pursuit monostatic pairs, if additional spatial prior is introduced. The proposed framework can be easily extended for multistatic configurations or external sources of scatterer's elevation.**

***Index Terms*—SAR tomography, Tandem-L, TanDEM-X, synthetic aperture radar (SAR).**

I. Introduction

A. Motivation

BISTATIC or multistatic configuration is a prominent feature of various future synthetic aperture radar (SAR) satellite missions. Some of these missions can be summarized as follows.

- Tandem-L, a German satellite mission concept whose primary goal is to observe the dynamic processes on earth's surface in high resolution with an unprecedented accuracy [1]. It comprises two satellites (e.g., TL-1 and TL-2). Each of them will have on board a high-resolution wide-swath L-band SAR. Basically, these two satellites will fly in close formation and operate in bistatic mode. This mode utilizes either TL-1 or TL-2 as a transmitter to illuminate a common radar footprint, while both receive radar echoes from earth's surface. In addition, a bidirectional radio frequency (RF) link is necessary for a highly accurate mutual time and phase referencing. This requirement will be easily fulfilled by means of the heritage of the TanDEM-X (TerraSAR-X add-on for Digital Elevation Measurements) mission [2]. Due to limited temporal decorrelation and atmospheric phase screen (APS), single-pass bistatic interferograms are characterized by better phase quality as compared to conventional repeat-pass ones and thus are more suitable for generating a global, consistent and high-resolution digital elevation model [3].
- SAOCOM-CS, a bistatic mission concept attaching to SAOCOM a passive companion SAR satellite operating in L-band [4].
- SEntinel-1 SAR Companion Multistatic Explorer (SESAME), a bistatic mission concept adding to Sentinel-1 two passive companion SAR satellites operating in C-band [5].
- Sentinel-1 "tandem" (i.e., one-day separation) or bistatic mission concept involving the prospective Sentinel-1C and another satellite from the series [6].
- High Resolution Wide Swath (HRWS), the successor of TerraSAR-X comprising one or two SAR satellites operating in X-band [7], [8], and possibly several additional passive companion transponder satellites without bidirectional phase synchronization link (MirrorSAR) [9]–[11].

Above all, Tandem-L is the most intriguing mission to us, not only because it is the one and only concept that has already undergone very comprehensive and intensive studies (see for example [12]–[16] and the references therein), but it is also extremely promising for a huge variety of geophysical applications.

In this paper, we address the problem of spaceborne differential SAR tomography (D-TomoSAR, see for instance [17]–[23]) in urban areas using bistatic or pursuit monostatic data. The latter, on the contrary, requires two satellites in close formation to operate *independently* from each other [2]. It can be employed as a backup solution in case pulse or phase synchronization fails. Given a temporal baseline of a few seconds and a moderate wind speed, the temporal decorrelation is still small for most terrain types including vegetation and atmospheric path delays can be assumed to cancel each other out during interferometric processing [24]. Hereafter we refer to bistatic and pursuit monostatic collectively as "bistatic-like".

We propose an austere framework which 1) reconstructs the elevation dimension with only bistatic-like interferograms, and subsequently 2) uses this as deterministic prior to estimate deformation parameters with conventional repeat-pass interferograms generated from bistatic-like pairs. Note that 1) is essentially a non-differential TomoSAR subproblem. We will refer to 2) as the DefoSAR subproblem. For point-like scatterers, the advantages of this framework are at least two-

This work is jointly supported by Helmholtz Association under the framework of the Young Investigators Group "SiPEO" (VH-NG-1018, www.sipeo.bgu.tum.de), DLR Space Administration under the project "J Lo—The Joy of Long Baselines" in the frame of "Entwicklung von innovativen wissenschaftlichen Methoden und Produkten im Rahmen der TanDEM-X Science Phase", the European Research Council (ERC) under the European Unions Horizon 2020 research and innovation programme (grant agreement No. [ERC-2016-StG-714087], acronym: *So2Sat*), and the Bavarian Academy of Sciences and Humanities in the framework of Junges Kolleg. *Corresponding author: Xiao Xiang Zhu.*

N. Ge is with the Remote Sensing Technology Institute (IMF), German Aerospace Center (DLR), 82234 Wessling, Germany (e-mail: Nan.Ge@dlr.de).

X. X. Zhu is with the Remote Sensing Technology Institute (IMF), German Aerospace Center (DLR), 82234 Wessling, Germany, and with Signal Processing in Earth Observation (SiPEO), Technical University of Munich (TUM), 80333 Munich, Germany (e-mail: xiaoxiang.zhu@dlr.de).

fold: a) the (almost) APS-free nature of bistatic-like interferograms leads to better elevation reconstruction, and in turn to more accurate deformation estimation; b) the dimension of the original problem is downscaled multiplicatively in each subproblem, which increases on the whole the algorithmic efficiency. For distributed scatterers, adaptive multilooking can be employed to increase their signal-to-noise ratio (SNR) to the level of point-like ones [25]–[27]. Therefore, the same arguments also apply. Besides, the elevation reconstruction of distributed scatterers relies less on the performance of adaptive multilooking, since their decorrelation is much less severe in bistatic-like interferograms than in conventional repeat-pass ones.

For the purpose of a practical demonstration, we use TanDEM-X—to date the sole civil spaceborne bistatic or multistatic mission—data in pursuit monostatic mode.

The proposed framework is envisioned to be incorporated into our Tandem-L processing chain. As one would expect, it is, with up to some minor adaptation, directly applicable to other prospective bi- or multistatic missions.

B. Notations and structure

We adopt the following mathematical notations throughout the whole paper. Scalars are denoted as lower- or uppercase letters, e.g., r, N, λ. Vectors are denoted as bold lowercase letters, e.g., $\mathbf{b}$, $\boldsymbol{\gamma}$. Their elements are denoted as lowercase letters with subscript, e.g., the n-th entry of $\mathbf{g}$ is denoted as g_n. For vectors, $\|\cdot\|_2$ and $\|\cdot\|_1$ denote the ℓ_2 and ℓ_1 norm, respectively. The supports of any vector $\boldsymbol{\beta}$, i.e., the index set of all nonzero entries of $\boldsymbol{\beta}$, are denoted as $\mathrm{supp}(\boldsymbol{\beta})$. Matrices and sets are denoted as bold uppercase letters, e.g., $\mathbf{R}$, $\boldsymbol{\Omega}$. Single rows of matrices are denoted as bold lowercase letters with superscript, e.g., the n-th row of $\mathbf{R}$ is denoted as $\mathbf{r}^n$. For matrices, $\|\cdot\|_{\mathrm{F}}$ and $\|\cdot\|_{1,2}$ denote the Frobenius and $\ell_{1,2}$ norm, respectively. For any set $\boldsymbol{\Omega}$, $|\boldsymbol{\Omega}|$ denotes its cardinality and $2^{\boldsymbol{\Omega}}$ its power set, i.e., the set of all subsets of $\boldsymbol{\Omega}$, including $\boldsymbol{\Omega}$ itself and the empty set $\varnothing$. The sets of integers, real and complex numbers are denoted as $\mathbb{Z}$, $\mathbb{R}$, $\mathbb{C}$, respectively. Their nonnegative subsets are denoted with the subscript $+$, e.g., $\mathbb{Z}_+$ denotes the set of nonnegative integers.

The remainder of this paper is organized as follows. Sec. II introduces the aforementioned framework together with a theoretical analysis of its performance and complexity. This is followed by Sec. III where an empirical experiment with TanDEM-X pursuit monostatic data can be found. Sec. IV concludes this paper.

II. The TomoSAR and DefoSAR framework

As briefly mentioned in Sec. I, we divide the original differential TomoSAR problem using bistatic-like data sets into two ordered subproblems, namely (non-differential) TomoSAR and DefoSAR. In the TomoSAR subproblem, the elevation dimension is reconstructed with only bistatic-like interferograms. Subsequently, the reconstructed elevation position of each scatterer is used as deterministic prior in the DefoSAR subproblem, where its deformation parameters are estimated with conventional repeat-pass interferograms. These two categories of interferometric combinations are illustrated in Fig. 1.

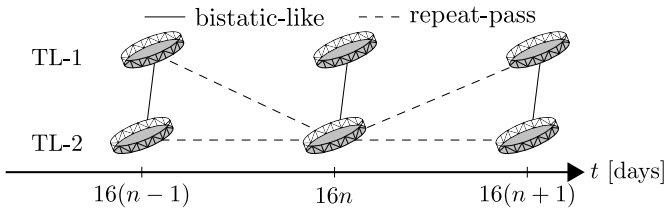

Fig. 1. A sketch of bistatic-like (solid lines) and conventional repeat-pass (dashed lines) interferometric combinations of future Tandem-L acquisitions. Bistatic-like pairs will be acquired repeatedly by TL-1 and TL-2 every 16 days.

A. TomoSAR

Given N coregistered bistatic-like complex interferograms, we aim to reconstruct the reflectivity profile along elevation.

For small N, however, the distribution of cross-track perpendicular baselines could be one-sided (see for example Fig. 2a). In this case, we propose to flip the sign of some of the baselines in order to maximize the standard deviation of their distribution. The rationale is to achieve a more uniform sampling of elevation frequencies [28], as well as a better Cramér-Rao lower bound on the error of elevation estimates [29]. Let $\mathbf{b} \in \mathbb{R}^N$ denote the vector of cross-track perpendicular baselines, the aforementioned problem can be formulated as

$$\underset{\mathbf{z}\in\{-1,+1\}^N}{\text{maximize}}\ \sigma(\mathbf{b}\odot\mathbf{z}), \tag{1}$$

where $\sigma : \mathbb{R}^N \to \mathbb{R}_+$ maps a vector to the sample standard deviation of its entries, and $\odot$ denotes the Hadamard product. Problem (1) is equivalent to

$$\underset{\mathbf{z}\in\{-1,+1\}^N}{\text{minimize}} -\left\|\mathbf{b}\odot\mathbf{z}-\mathbf{b}^{\mathrm{T}}\mathbf{z}/N\right\|_2^2, \tag{2}$$

which has two optimum points given unique entries of $\mathbf{b}$: suppose $\mathbf{z}^*$ is one of them, then $-\mathbf{z}^*$ is the other. Since N is small, we solve (2) by exhaustive search. In the unlikely case of one-sided baseline distribution with large N, the following heuristic can be adopted: sort baselines by their magnitude, choose a sign for the largest one in magnitude, set the second largest one to have the opposite sign, and so forth till all N baselines are exhausted. Accordingly, the signs of elevation frequency and interferometric phase are also flipped.

The optional sign flipping procedure is followed by layover separation. By the first-order Born approximation, far-field diffraction is often modeled as the integration of a phase-modulated elevation-dependent reflectivity profile (see for example [19]). After discretizing the elevation dimension and replacing integration with finite sum, bistatic-like InSAR observations $\mathbf{g} \in \mathbb{C}^N$ of a resolution cell can be approximated with the linear model $\mathbf{g} \approx \mathbf{R}\boldsymbol{\gamma}$, where $\mathbf{R} \in \mathbb{C}^{N\times L}$ is the TomoSAR design matrix, and $\boldsymbol{\gamma} \in \mathbb{C}^L$ denotes the discrete reflectivity profile along elevation. The n-th entry g_n of $\mathbf{g}$ is sampled at the elevation frequency $\xi_n \coloneqq 2b_n/(\lambda r)$, where b_n is the corresponding cross-track perpendicular baseline (after sign flipping), λ denotes the radar carrier wavelength, and r is the slant-range distance in the master acquisition. Let $\mathbf{s} \in \mathbb{R}^L$ denote the discretization of the elevation dimension, the n-th row of $\mathbf{R}$ is defined as $\mathbf{r}^n \coloneqq \exp(-j2\pi\xi_n\mathbf{s})$, where exp

operates elementwise. There exist numerous methods which estimate $\boldsymbol{\gamma}$ with given $\mathbf{R}$ and $\mathbf{g}$. Under the assumption that $\boldsymbol{\gamma}$ is sparse (i.e., its cardinality is small), a common approach is to solve the following ℓ_1-regularized least squares problem [30]

$$\hat{\boldsymbol{\gamma}} \coloneqq \arg\min_{\boldsymbol{\gamma}} \frac{1}{2}\|\mathbf{R}\boldsymbol{\gamma} - \mathbf{g}\|_2^2 + \lambda\|\boldsymbol{\gamma}\|_1, \tag{3}$$

where $\lambda > 0$ controls the trade-off between model goodness-of-fit and the sparsity of $\boldsymbol{\gamma}$. A similar formulation of (3) can be found in [31]. Despite its super-resolution power and robustness in terms of layover separation, ℓ_1 regularization is prone to spurious spikes. For this reason, it is often concatenated with model order selection which we state as follows [28]

$$\begin{aligned}\hat{\boldsymbol{\Omega}} \coloneqq &\arg\min_{\boldsymbol{\Omega}(,\boldsymbol{\beta})} \frac{1}{2}\|\mathbf{R}\boldsymbol{\beta} - \mathbf{g}\|_2^2 + \mathrm{C}(|\boldsymbol{\Omega}|) \\ &\text{subject to } \operatorname{supp}(\boldsymbol{\beta}) = \boldsymbol{\Omega} \subseteq \operatorname{supp}(\hat{\boldsymbol{\gamma}}),\end{aligned} \tag{4}$$

where $|\boldsymbol{\Omega}|$ denotes the cardinality of the index set $\boldsymbol{\Omega}$, $\mathrm{C} : \mathbb{Z}_+ \to \mathbb{R}_+$ evaluates the model complexity according to, e.g., Bayesian or Akaike information criterion (see [28] and the references therein), and $\operatorname{supp}(\boldsymbol{\beta}) = \{i \mid \beta_i \neq 0, i = 1, \ldots, L\}$, i.e., it is the set of the indices of nonzero entries or supports in $\boldsymbol{\beta}$. The constraint in (4) renders the supports of the final reflectivity profile estimate a subset of those of $\hat{\boldsymbol{\gamma}}$, and therefore allows outlier mitigation. Note that the underestimated amplitude is hereby debiased as a by-product.

In the next subsection, we introduce the DefoSAR subproblem which uses as deterministic prior the elevation estimates of single or multiple scatterers from TomoSAR reconstruction.

B. DefoSAR

Given $2N-2$ coregistered conventional repeat-pass complex interferograms generated from N bistatic-like pairs (see Fig. 1), and the elevation estimates $\hat{\mathbf{s}} \coloneqq \mathbf{s}_{\hat{\boldsymbol{\Omega}}}$ of a total number of $K \coloneqq |\hat{\boldsymbol{\Omega}}|$ scatterers, our objective is to reconstruct their deformation by means of a composite model.

For single point-like scatterers (i.e., no layover effect), the elevation estimates can be straightforwardly converted into topographic phase and compensated in the conventional repeat-pass interferograms. A similar approach for distributed scatterers can be found in [32].

In a more general sense, $\hat{\mathbf{s}}$ can be considered as deterministic prior. Let $\boldsymbol{\Psi} \coloneqq \{\boldsymbol{\psi}_m\}$ denote a set of M basis functions which are parametrized by the temporal baseline t_n and employed to model scatterer's deformation, and $\mathbf{c}_m \in \mathbb{R}^{|\mathbf{c}_m|}$ be the discretization of the unknown coefficient of $\boldsymbol{\psi}_m$, we can construct the DefoSAR design matrix $\tilde{\mathbf{R}}(\hat{\mathbf{s}}, \boldsymbol{\Psi}) \in \mathbb{C}^{(2N-2)\times\tilde{L}}$, where $\tilde{L} \coloneqq K\prod_{m=1}^{M}|\mathbf{c}_m|$. Its n-th row can be expressed as $\tilde{\mathbf{r}}^n \coloneqq \exp(-j2\pi\xi_n\hat{\mathbf{s}}) \otimes \exp(-j(4\pi/\lambda)\boldsymbol{\psi}_1(t_n)\mathbf{c}_1) \otimes \cdots \otimes \exp(-j(4\pi/\lambda)\boldsymbol{\psi}_M(t_n)\mathbf{c}_M)$, where ξ_n is the elevation frequency of the n-th conventional repeat-pass interferogram with cross-track perpendicular baseline b_n, and $\otimes$ denotes the Kronecker product. Likewise, the repeat-pass InSAR observations $\tilde{\mathbf{g}} \in \mathbb{C}^{2N-2}$ of the same resolution cell can be approximated by $\tilde{\mathbf{g}} \approx \tilde{\mathbf{R}}(\hat{\mathbf{s}}, \boldsymbol{\Psi})\tilde{\boldsymbol{\gamma}}$, where $\tilde{\boldsymbol{\gamma}} \in \mathbb{C}^{\tilde{L}}$ denotes the discrete reflectivity profile along elevation and deformation. The coefficients of deformation basis functions can be estimated with a variant of non-linear least squares [22] which additionally constrains $\tilde{\boldsymbol{\gamma}}$ to have exactly one nonzero entry at each elevation position in $\hat{\mathbf{s}}$. In order to avoid overfitting, we propose furthermore to perform deformation model order selection. Let $2^{\boldsymbol{\Psi}}$ be the power set of $\boldsymbol{\Psi}$, i.e., all possible combinations of deformation basis functions including the non-differential case represented by the null set $\varnothing$, the deformation model order selection problem can be cast as

$$\begin{aligned}\hat{\boldsymbol{\Theta}} \coloneqq &\arg\min_{\boldsymbol{\Theta}\subseteq 2^{\boldsymbol{\Psi}}(,\tilde{\boldsymbol{\beta}})} \frac{1}{2}\|\tilde{\mathbf{R}}(\hat{\mathbf{s}}, \boldsymbol{\Theta})\tilde{\boldsymbol{\beta}} - \tilde{\mathbf{g}}\|_2^2 + \mathrm{C}(|\boldsymbol{\Theta}|) \\ &\text{subject to } |\operatorname{supp}(\tilde{\boldsymbol{\beta}})| = |\operatorname{supp}(\mathfrak{I}(\tilde{\boldsymbol{\beta}}))| = |\hat{\boldsymbol{\Omega}}|,\end{aligned} \tag{5}$$

where $\mathfrak{I} : \mathbb{C}^{\tilde{L}} \to \mathbb{C}^{K}$ integrates over each deformation coefficient. The constraint in (5) enforces that the discrete reflectivity profile in the elevation-deformation domain, and the one in the (integrated) elevation domain share the same number of supports, which leads to the previously mentioned desired effect. Again, we solve this subproblem by exhaustive search. In the case of a highly complex composite model, we can proceed in a greedy manner: choose from the remaining scatterers the one with the strongest power, rebuild the DefoSAR design matrix, find the best fit in terms of penalized likelihood (5), and subtract it from the residues of $\tilde{\mathbf{g}}$, etc.

Assuming that the elevation estimate of a single scatterer is perfect, the Cramér-Rao lower bound (CRLB) on the error of the coefficient estimate $\hat{c}$ of a single basis function ψ is

$$\sigma_{\hat{c}} \coloneqq \frac{\lambda}{4\pi\sqrt{2N-2}\sqrt{2SNR}\,\sigma_{\psi}}, \tag{6}$$

where σ_ψ is the standard deviation of ψ evaluated at different t_n, i.e., $\psi(t_1), \ldots, \psi(t_{2N-2})$. A proof of (6) is given in the appendix.

In a nutshell, our proposed framework can be summarized as follows. A simple theoretical analysis is provided in the next subsection.

Algorithm 1 Tomo- and DefoSAR

TomoSAR Input: cross-track perpendicular baselines $\mathbf{b}$, elevation frequencies $\{\xi_n\}$, bistatic-like InSAR observations $\mathbf{g}$

1: (optional) sign flipping (2)
2: sparse reconstruction (3)
3: model order selection for elevation estimation (4)

TomoSAR Output: elevation estimates $\hat{\mathbf{s}}$

DefoSAR Input: $\hat{\mathbf{s}}$, temporal baselines $\{t_n\}$, deformation basis functions $\boldsymbol{\Psi}$, repeat-pass InSAR observations $\tilde{\mathbf{g}}$

4: if $|\hat{\mathbf{s}}| \neq \varnothing$, deformation model order selection (5)

DefoSAR Output: selected deformation basis functions $\hat{\boldsymbol{\Theta}}$ and their estimated coefficients

C. Tomo- and DefoSAR vs. D-TomoSAR: a theoretical analysis

Now we analyze the performance and complexity of the proposed framework from a theoretical point of view.

We start with a proof that

Case 1 (pursuit monostatic): the proposed framework has a tighter theoretical bound, and

Case 2 (bistatic): its CRLB is no worse by a factor of 2.

In order to simplify the argument, suppose without loss of generality that N bistatic-like pairs are coregistered with a redundant master scene that is not used in tomographic processing. Thereby $2N$ (instead of $2N-1$ if we count the interferogram in the middle of Fig. 1 as a repeat-pass one with zero temporal baseline) conventional repeat-pass interferograms are generated from these pairs. Note that this assumption certainly favors the D-TomoSAR approach.

For TomoSAR using N bistatic-like pairs, the CRLB on the elevation estimate $\hat{s}$ of a single scatterer is [29]

$$\sigma_{\hat{s}} \coloneqq \frac{\lambda r}{4\pi\sqrt{N}\sqrt{2SNR}\,\sigma_b}, \tag{7}$$

where σ_b is the standard deviation of the perpendicular baselines $\{b_n\}$ of the N bistatic-like pairs. On the other hand, D-TomoSAR uses as inputs $2N$ conventional repeat-pass interferograms that are generated from the N bistatic-like pairs. For a single scatterer, suppose that its deformation time series is described by a basis function ψ. It can be shown that the CRLB on its elevation estimate is

$$\tilde{\sigma}_{\hat{s}} \coloneqq \frac{\lambda r}{4\pi\sqrt{2N}\sqrt{2SNR}\,\sqrt{1-\rho^2}\sigma_{\tilde{b}}}, \tag{8}$$

where $\sigma_{\tilde{b}}$ is the standard deviation of the perpendicular baselines $\{\tilde{b}_n\}$ of the $2N$ conventional repeat-pass interferograms, and ρ denotes the correlation coefficient between $\tilde{b}_n$ and $\psi_n \coloneqq \psi(t_n)$. The proof of (8) is similar to that of (6) with one minor difference: s is considered here as an unknown and therefore the corresponding Fisher information matrix is in $\mathbb{R}^{4\times 4}$.

We assume that $\{\tilde{b}_n\}$ are independent and identically distributed random variables.

Case 1 (pursuit monostatic):

For each b_n, there exist unique $k, l \in \mathbb{Z}_+$, $1 \le k \ne l \le 2N$, such that $b_n = \tilde{b}_k - \tilde{b}_l$. It follows that $\sigma_b^2 = 2\sigma_{\tilde{b}}^2$. For example, suppose that each $\tilde{b}_n$ is uniformly distributed in $[-b_{\max}, +b_{\max}]$, $b_{\max} > 0$. This implies that $\sigma_{\tilde{b}}^2 = (b_{\max})^2/3$. As a result, each b_n follows a symmetric triangular distribution with $\sigma_b^2 = 2(b_{\max})^2/3$. Dividing $\sigma_{\hat{s}}$ by $\tilde{\sigma}_{\hat{s}}$ yields

$$\frac{\sigma_{\hat{s}}}{\tilde{\sigma}_{\hat{s}}} = \sqrt{1-\rho^2} < 1. \tag{9}$$

Case 2 (bistatic):

From $b_n = (\tilde{b}_k - \tilde{b}_l)/2$ it follows that $\sigma_b^2 = \sigma_{\tilde{b}}^2/2$ and consequently $\sigma_{\hat{s}}/\tilde{\sigma}_{\hat{s}} < 2$, which completes the proof.

Note that similar results can be obtained for deformation parameter estimate.

Furthermore, we analyze the complexity of the proposed framework via flop count. In the case of a one-sided distribution of cross-track perpendicular baselines, the optional sign flipping problem (2) can be solved using exhaustive search in $\mathcal{O}(N2^{N-1})$ flops. For large N, the heuristic approach, which is based on a simple sorting, can be performed in $\mathcal{O}(N \log N)$ flops.

The sparse reconstruction problem (3) can be solved using the alternating direction method of multipliers [33] in $\mathcal{O}(LNT)$ flops[1], assuming that $N \ll L$ and $N \ll T$, where T is the number of iterations. The model order selection problem for elevation estimates (4) is essentially a series of subset least squares problems that can be solved in $\mathcal{O}(N)$ flops. The deformation model order selection problem (5) can be solved in $\mathcal{O}(N\tilde{L}^K)$ flops, or $\mathcal{O}(N\tilde{L})$ flops using the greedy approach. Therefore, the total cost of the proposed framework is at most $\mathcal{O}(LNT + N\tilde{L}^K)$ flops.

As a comparison, the total cost of applying the sparse reconstruction and model order selection directly to $2N$ repeat-pass interferograms is $\mathcal{O}(L\tilde{L}NT)$ flops. By assuming that $L \approx \tilde{L} \ll T$, the proposed framework is approximately $\tilde{L}$ times as simple (as opposed to complex) for single and double scatterers, which are considered as the most common cases in urban areas [34].

In Sec. III, we demonstrate the applicability of the proposed framework with a stack of TanDEM-X pursuit monostatic acquisitions.

III. Experiments with TanDEM-X Pursuit Monostatic Data

Due to the unavailability of suitable Tandem-L bistatic test data, we applied the proposed framework to a small TanDEM-X pursuit monostatic stack. The pursuit monostatic mode was temporarily put into practice from October 2014 to February 2015 during the TanDEM-X Science Phase [24]. In order to avoid RF interference between radar signals, the along-track distance was set to approximately 76 km, which corresponds to a temporal baseline of circa 10 seconds. During this five-month period, 12 staring spotlight scenes of the City of Las Vegas were acquired. Out of these, 6 pursuit monostatic interferograms were generated and their baselines are plotted in Fig. 2a. As can be observed, relatively large values in magnitude are available, whereas in the usual cases of TSX and TDX[2] the baselines are bounded between ± 250 m. As a matter of fact, in order to favor TomoSAR and other applications in polar regions, cross-track perpendicular baselines were programmed to slowly drift (in magnitude) from 0 to 750 m [24]. Since all baselines but one are negative, we applied the sign flipping procedure that was introduced in Sec. II-A. The baselines after sign flipping are plotted in Fig. 2b. The sign was indeed flipped for two baselines and the standard deviation increased from approximately 286.7 to 308.3 m. As a consequence, the CRLB was improved by 7.5%.

As a practical demonstration of the proposed framework, we focus on a small area which contains a high-rise building and is therefore subject to layover. The APS was compensated by subtracting the phase of a nearby ground reference point in each interferogram. This step is also known as phase calibration [35], [36]. Given a sufficiently large number of bistatic-like pairs (for example $N \ge 11$), a stack of $2N-1$ repeat-pass interferograms can be generated. Subsequently, a standard persistent scatterer interferometry (PSI) approach

[1]For the sake of simplicity, we count each complex addition or multiplication as one flop.

[2]In this context we refer to the two satellites in the TanDEM-X mission as TSX and TDX.

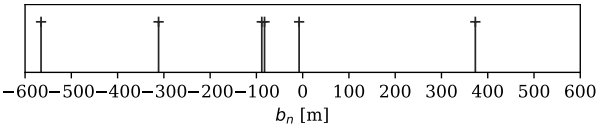

(a) Before sign flipping

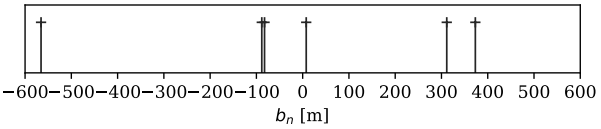

(b) After sign flipping

Fig. 2. Cross-track perpendicular baselines of 6 pursuit monostatic interferograms before (2a) and after sign flipping (2b). The height of ambiguity is approximately, in ascending order, 10, 15, 18, 64, 69 and 738 m.

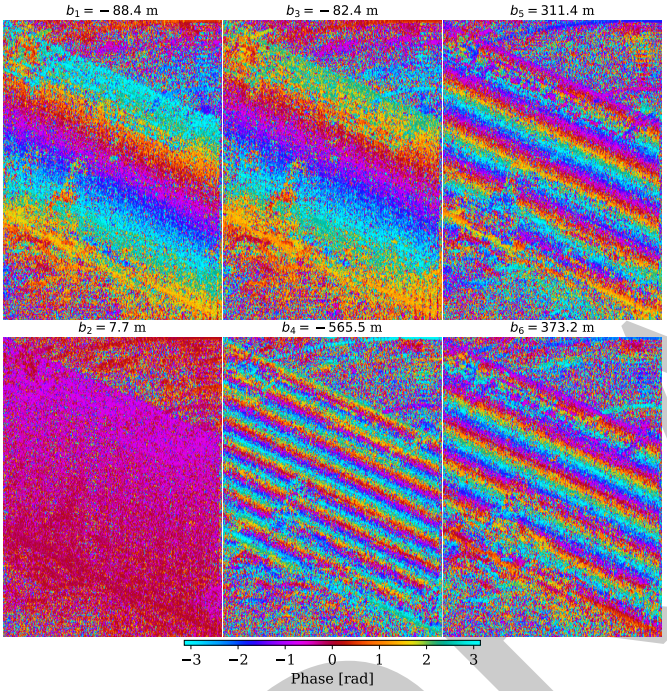

Fig. 3. Pursuit monostatic interferograms of a high-rise building, generated from 12 TSX and TDX acquisitions and annotated with their cross-track perpendicular baselines.

[37]–[39] can be applied to estimate the APS of single point-like scatterers. This can be resampled and compensated for the whole scene (see for example [40] and the references therein). Alternatively, topographic updates of single point-like scatterers can be first estimated using only bistatic-like interferograms and then compensated in conventional repeat-pass interferograms for APS estimation [32]. Fig. 3 shows the 6 pursuit monostatic interferograms of a high-rise building and its surroundings. Note that the fringes on the building facade appear to be highly coherent. For Tandem-L, we would expect even higher coherence, especially for distributed scatterers. This is due to minimized temporal decorrelation in the bistatic mode, as well as the outstanding penetration depth in L-band.

In the next subsection, the sparse reconstruction is enhanced by exploiting joint sparsity among different resolution cells, in order to circumvent the issue of the extremely small number of pursuit monostatic pairs.

A. Joint sparsity reconstruction for extremely small N

Although the pursuit monostatic interferograms in Fig. 3 are mostly unaffected by APS or temporal decorrelation, the number of elevation frequencies (i.e., 6) is extremely small. Zhu et al. reported that, for $N = 6$, not exploiting special signal structure can lead to results that are subject to outliers [41]. With the objective of achieving high-quality elevation reconstruction, we introduced spatial prior in the form of iso-height line segments along range on the building facade. The iso-height line segments were derived from freely available geospatial data containing building footprints. All resolution cells in a given line segment form an iso-height cluster, which was jointly reconstructed. In other words, we solve instead the $\ell_{1,2}$-regularized least squares problem

$$\hat{\mathbf{\Gamma}} \coloneqq \arg\min_{\mathbf{\Gamma}} \frac{1}{2}\|\mathbf{R}\mathbf{\Gamma} - \mathbf{G}\|_{\mathrm{F}}^2 + \lambda\|\mathbf{\Gamma}\|_{1,2}, \tag{10}$$

where the p-th column of $\mathbf{\Gamma} \in \mathbb{C}^{L\times P}$ represents the discrete reflectivity profile in the p-th resolution cell (also known as snapshot) along the iso-height line segment, the p-th column of $\mathbf{G} \in \mathbb{C}^{N\times P}$ contains the InSAR observations of the p-th resolution cell, $\|\cdot\|_{\mathrm{F}}$ denotes the Frobenius norm, and $\|\cdot\|_{1,2}$ denotes $\ell_{1,2}$ norm, i.e., $\|\mathbf{\Gamma}\|_{1,2} \coloneqq \sum_{i=1}^{L}\|\boldsymbol{\gamma}^i\|_2$. A treatise on this algorithm can be found in [41], where it was shown empirically that solving the $\ell_{1,2}$-regularized least squares problem (10) with N interferograms and P snapshots achieves almost the same performance, in terms of elevation estimate error, as solving the ℓ_1-regularized least squares problem (3) with NP interferograms. Similar approaches using multiple snapshots can be found in, e.g., [42], [43]. Subsequently, the model order selections (4) and (5) were performed individually for each resolution cell.

Fig. 4 shows the mean intensity map of the building of interest and several exemplary iso-height line segments. The height estimates of single and layover scatterers are plotted in Fig. 5. Roof interacts with facade and ground in the near range, while facade and ground are subject to layover in the far range. The smooth color transition from near to far range indicates a good quality of height estimates. Nevertheless, there are indeed a few outliers in the far range. These outliers, which we managed to reproduce with simulated data sets, are presumably due to the yet nonuniform distribution of the extremely small number of baselines. The height profile, generated via averaging within each iso-height cluster, can be found in Fig. 6, where roof and facade are clearly identifiable. In order to assess the relative accuracy of height estimates, we extracted the point cloud segment corresponding to facade by thresholding of point density [44] and fitted a vertical plane with ℓ_1-loss (see Fig. 7). From the bird's-eye view, all scatterers appear to be evenly distributed w.r.t. the fitted facade plane. We calculated the elevation distance of each scatterer's estimated position to the facade plane, and projected it into the vertical direction. We refer to this vertical component as the height estimate error relative to the fitted vertical plane. Its histogram resembles a zero-mean normal distribution (see Fig. 8). The relative vertical accuracy, which is defined in this context as the median absolute deviation (MAD) of height estimate error, was estimated to be approximately 0.29 m.

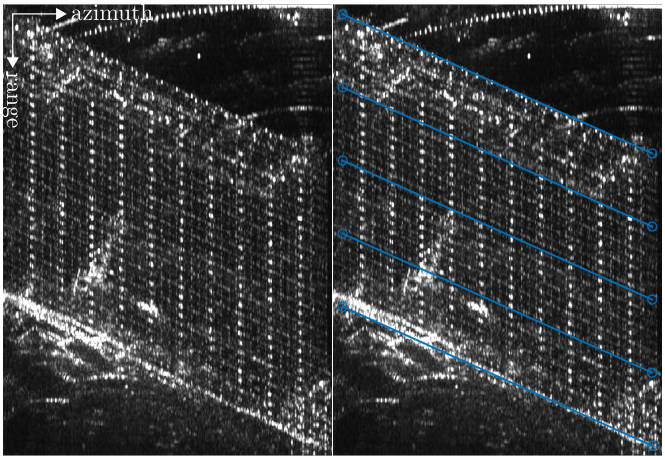

Fig. 4. Mean intensity map (left) and overlaying exemplary iso-height line segments (right).

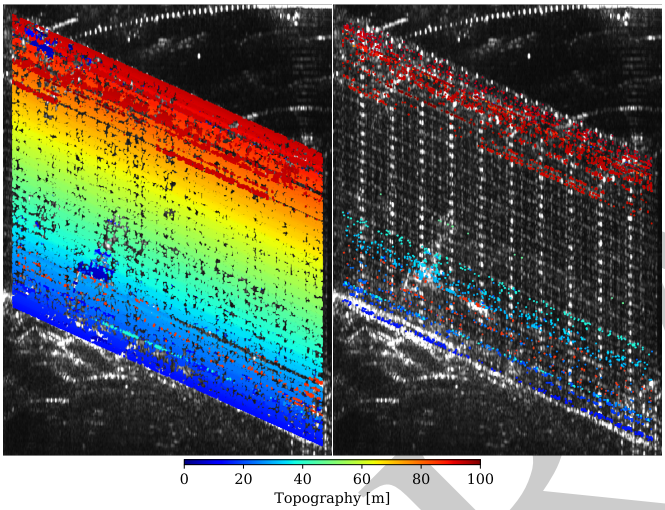

Fig. 5. Height estimates of single (left) and layover scatterers (right). In the case of layover, the height estimate of the highest scatterer is shown.

Note that this can be interpreted as an upper bound on the true relative vertical accuracy, since the building facade is not entirely flat.

As explained in Sec. II-B, these height estimates can be used as deterministic prior for repeat-pass interferometry. For single scatterers, the topographic phase was compensated by using the height-to-phase conversion factor (see Fig. 9). The residual phase is presumably mainly due to scatterer's motion and already reveals a pattern of it. Note that every pair of repeat-pass interferograms sharing the same temporal baseline (in days) appear almost identical after topographic phase compensation. This provides a compelling argument for limited temporal decorrelation and APS wihtin a pursuit monostatic pair. Needless to say, an increase in the coherence of prospective Tandem-L repeat-pass interferograms can be expected. Even for distributed scatterers, L-band signal is known to maintain a certain degree of coherence after more than two years of time [45], [46]. This would undoubtedly lead to a greater coverage of retrievable information. Given the span of temporal baselines of 132 days, the motion was assumed

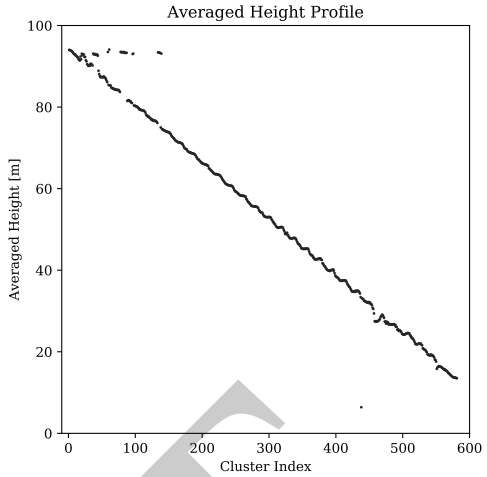

Fig. 6. Cluster-wise averaged height profile.

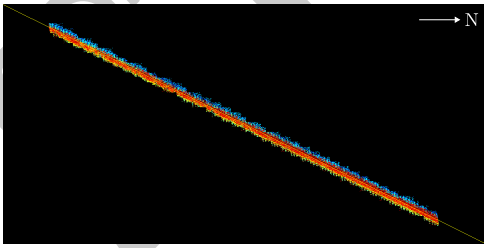

Fig. 7. Bird's-eye view of the point cloud segment corresponding to facade.

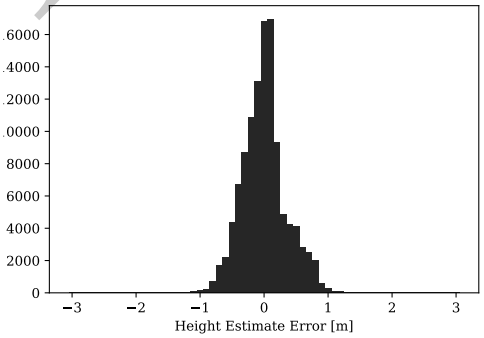

Fig. 8. Histogram of height estimate error relative to a fitted vertical plane. The median and MAD are approximately 0.00 and 0.29 m, respectively.

to consist primarily of thermal contraction and expansion due to temperature change (see for example [47]). To this end, a sinusoidal model was employed. By solving the DefoSAR subproblem (5), we obtained the amplitude estimates of periodical deformation for single and layover scatterers, which are shown in Fig. 10. In general, the amplitude of periodical deformation is positively correlated with height (see the scatter plot in Fig. 11) and relatively large in magnitude at the top of the building as well as at the side. This pattern accords with that of repeat-pass interferograms of single scatterers after topographic phase compensation in Fig. 9b, which partially validates our results.

A preliminary comparison with D-TomoSAR is provided in the next subsection.

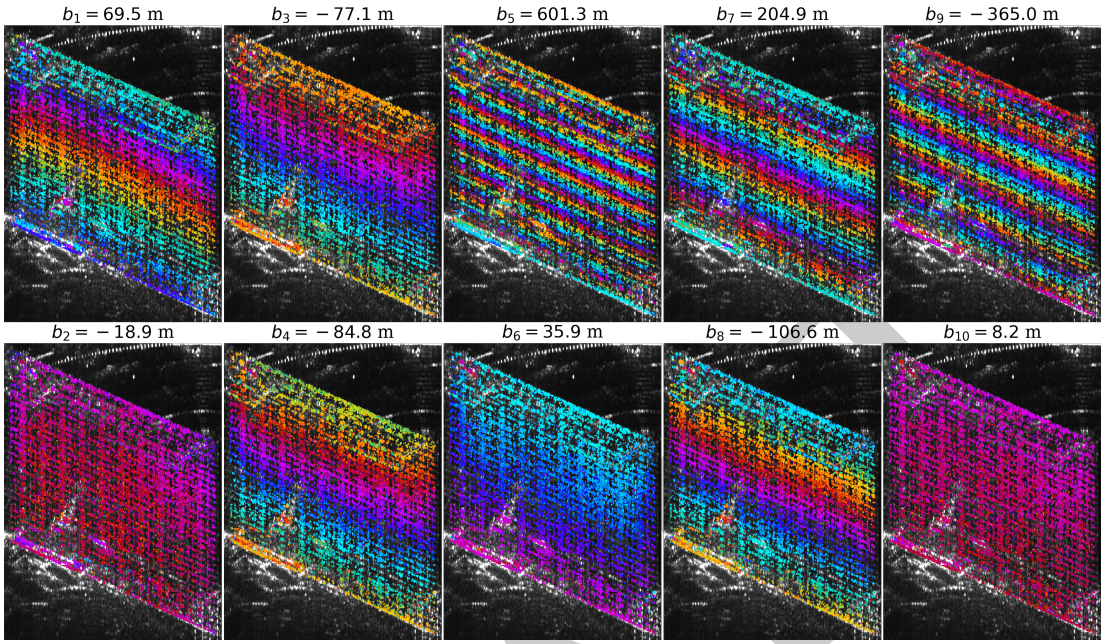

(a) Before topographic phase compensation

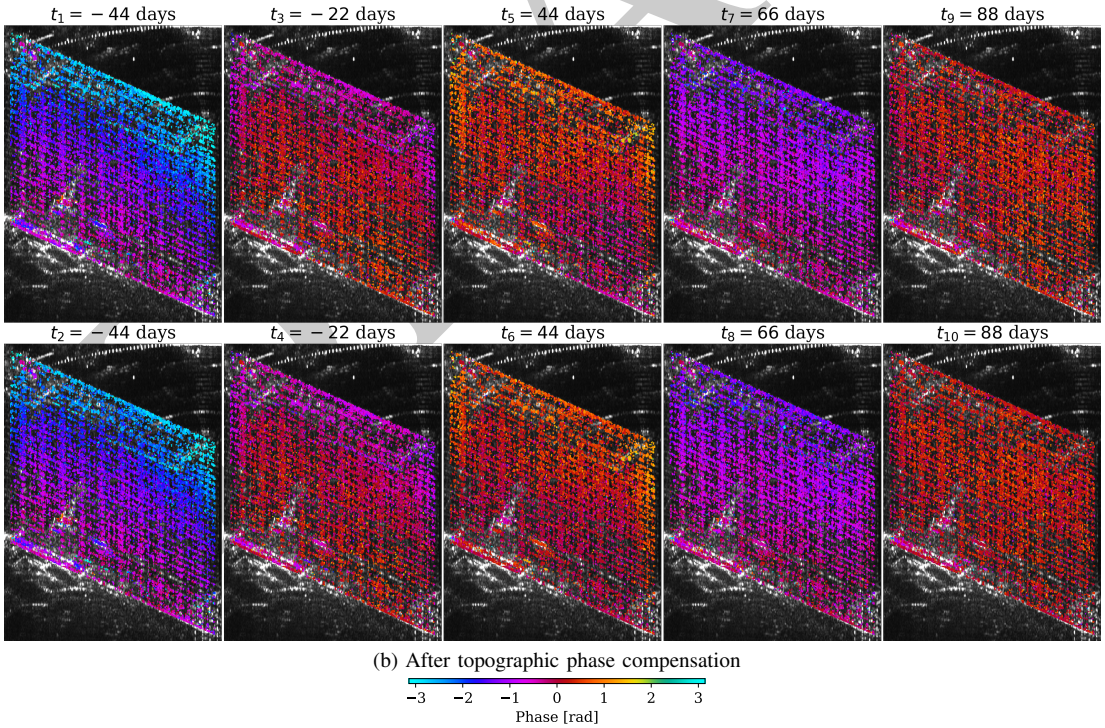

(b) After topographic phase compensation

Fig. 9. Repeat-pass interferometric phase of single scatterers before (9a) and after topographic phase compensation (9b), annotated with their cross-track perpendicular or temporal baselines.

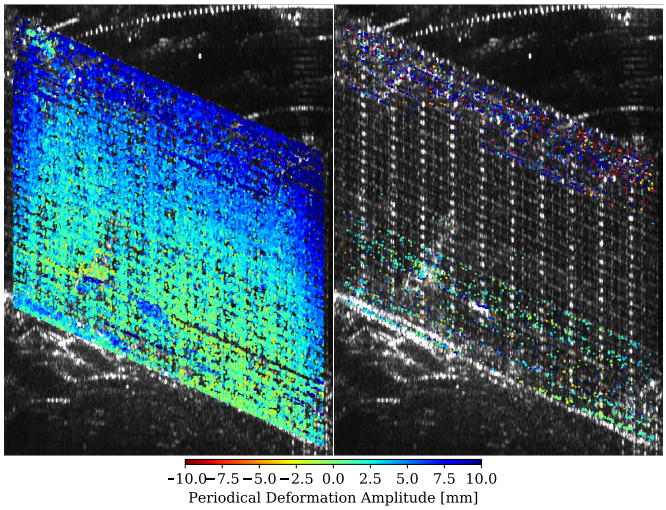

Fig. 10. Periodical deformation amplitude estimates of single (left) and layover scatterers (right). In the case of layover, the amplitude estimate of the highest scatterer is shown.

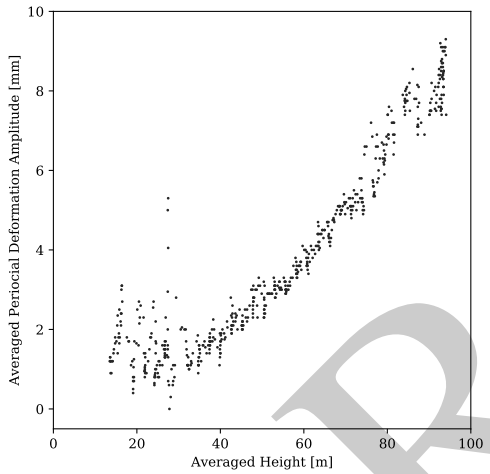

Fig. 11. Scatter plot of averaged height and periodical deformation amplitude.

B. Tomo- and DefoSAR vs. D-TomoSAR: an empirical analysis

In Sec. III-A, we introduced additional spatial prior in order to boost the sparse reconstruction for extremely small N. The joint sparsity reconstruction method (10) is, however, only applicable to bistatic-like data sets. Therefore, a direct comparison with the results generated by the same method using conventional repeat-pass interferograms is ruled out. For the sake of fairness, we employed the pixel-wise sparse reconstruction method (3) with identical parameter quantization for both TomoSAR and D-TomoSAR processing using 6 pursuit monostatic and 11 repeat-pass interferograms, respectively. As might be expected, the former was followed by DefoSAR processing for deformation parameter estimation. Tab. I summarizes the overall runtime on a desktop with a quad-core Intel processor at 3.40 GHz and 16 GB RAM. The Tomo- and DefoSAR framework was computationally approximately 6.4 times as efficient.

As listed in Tab. II, the standard deviation σ_b of the cross-track perpendicular baselines $\{b_n\}$ of the 6 pursuit monostatic

TABLE I
TOMO- AND DEFOSAR VS. D-TOMOSAR: RUNTIME

	Tomo- and DefoSAR	D-TomoSAR	Ratio
Runtime [h]	0.61	3.94	6.44

TABLE II
TOMOSAR VS. D-TOMOSAR: BASELINE STANDARD DEVIATION, $\sqrt{1-\rho^2}$ AND CRLB OF HEIGHT ESTIMATES ($SNR = 5$ DB)

	TomoSAR	D-TomoSAR	Ratio
Baseline σ [m]	308.31	226.33	1.36
$\sqrt{1-\rho^2}$	n.a.	0.92	n.a.
CRLB of height [m]	0.48	0.52	1.10

TABLE III
STATISTICS OF THE HEIGHT ESTIMATE ERROR IN FIG. 13

	TomoSAR	D-TomoSAR	Ratio
No. of scatterers	87595	91063	1.04
Median [m]	0.00	0.00	n.a.
Mean [m]	0.00	0.00	n.a.
MAD [m]	0.52	0.61	1.16
Standard Deviation [m]	0.50	0.58	1.16

interferograms is approximately 1.4 times as high as the one $\sigma_{\tilde{b}}$ of $\{\tilde{b}_n\}$ of the 11 repeat-pass interferograms. Note that our assumption in Sec. II-C implies that $\sigma_b = \sqrt{2}\sigma_{\tilde{b}}$. The correlation between $\tilde{b}_n$ and the deformation basis function ψ_n leads to $\sqrt{1-\rho^2} \approx 0.92$. This can be interpreted as a degradation of $\sigma_{\tilde{b}}$ by 8% at the expense of taking deformation into account. Given a single scatterer with an SNR of 5 dB, the CRLB of height estimates for the proposed framework is approximately 0.48 m, which is 1.1 times as low.

Same as in Sec. III-A, we extracted the point cloud segment corresponding to building facade by thresholding of the 2-D point density. This process also eliminated false alarms due to the extremely small number of interferograms. As shown in Fig. 12, both facade segments appear quite similar, except that the uppermost part of the facade is incomplete in the D-TomoSAR result. A possible explanation could be that the already complex short-distance roof-facade layover of point-like scatterers is furthermore complicated by their deformation behavior. The facade segment produced by D-TomoSAR has slightly more scatterers (see Tab. III), but we consider this difference to be insignificant. In order to access the quality of the point cloud, we followed the same approach that was introduced in the last subsection, namely to fit a vertical plane into each facade segment, project the distance of each point to the fitted plane into the vertical axis, and interpret it as the height estimate error relative to the fitted plane. The normalized histograms are shown in Fig. 13. While both histograms are centered around zero, the one of TomoSAR has less deviation. The MAD is in fact approximately 1.16 as low for TomoSAR (cf. 1.10 as predicted in Tab. II for an average SNR of 5 dB).

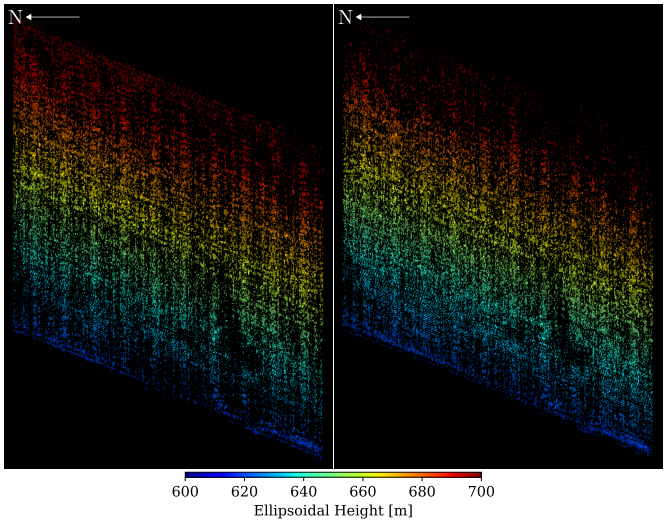

Fig. 12. Reconstructed facade segments (color-coded by ellipsoidal height). Left: TomoSAR using 6 pursuit monostatic interferograms. Right: D-TomoSAR using 11 repeat-pass interferograms.

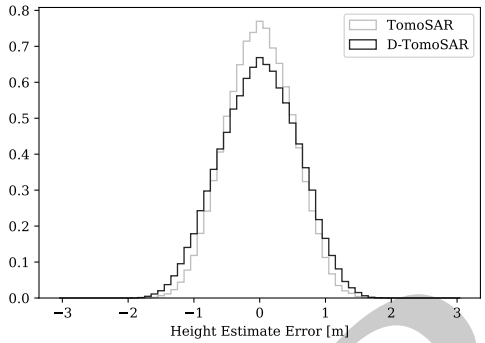

Fig. 13. Normalized histogram of height estimate error relative to a fitted vertical plane. Gray: TomoSAR using 6 pursuit monostatic interferograms. Black: D-TomoSAR using 11 repeat-pass interferograms. See Tab. III for more statistics.

IV. Conclusion

In the preceding sections, we tackled the problem of differential TomoSAR in urban areas using bistatic-like data sets, which will be delivered by the prospective Tandem-L mission as operational products. We proposed a framework which divides the original problem into two subsequent subproblems. The first subproblem is essentially non-differential TomoSAR with bistatic-like interferograms and can be dealt with using already existing methods. In the second subproblem, elevation estimates are incorporated as deterministic prior into the DefoSAR design matrix in order to estimate the coefficients of deformation basis functions with conventional repeat-pass interferograms. We showed via theoretical and empirical analyses that this framework, when applied to pursuit monostatic data, not only outperforms standard D-TomoSAR but is also less expensive. In an extreme case, we applied our framework to merely 6 TanDEM-X pursuit monostatic pairs and achieved reasonable results for both elevation and deformation estimates. The relative vertical accuracy of the resulted point cloud was estimated to be approximately 0.29 m.

Although we proposed to estimate each scatterer's elevation position using bistatic-like interferograms, it could indeed stem from other sources such as ray-tracing simulation with an external 3-D building model [48] or with one reconstructed from a single SAR intensity image [49]. The corresponding minor adaptation would extend the applicability of the proposed framework to interferometric stacks composed of nothing but conventional repeat-pass acquisitions and thereby allow precise object-based infrastructure monitoring.

Appendix
Proof of (6)

First we state the following result from [50].

Suppose that $\mathbf{x} \in \mathbb{R}^L$ and $\mathbf{y} \in \mathbb{C}^N$ are the parameter and data vectors, respectively, and $\mathbf{y}$ is the random Gaussian observation of the deterministic signal vector $\mathbf{u}(\mathbf{x}) \in \mathbb{C}^N$ with covariance matrix $\mathbf{C}_\mathbf{y}(\mathbf{x})$. The likelihood function is

$$f(\mathbf{y} \mid \mathbf{x}) \coloneqq \frac{1}{\pi^N \det\left(\mathbf{C}_\mathbf{y}(\mathbf{x})\right)} \cdot \exp\left(-\big(\mathbf{y}-\mathbf{u}(\mathbf{x})\big)^{\mathrm{H}} \mathbf{C}_\mathbf{y}^{-1}(\mathbf{x}) \big(\mathbf{y}-\mathbf{u}(\mathbf{x})\big)\right).$$

It can be shown that the Fisher information matrix $\mathbf{I}(\mathbf{x})$ is given by

$$[\mathbf{I}(\mathbf{x})]_{kl} \coloneqq \operatorname{tr}\left(\mathbf{C}_\mathbf{y}^{-1}(\mathbf{x}) \frac{\partial \mathbf{C}_\mathbf{y}(\mathbf{x})}{\partial x_k} \mathbf{C}_\mathbf{y}^{-1}(\mathbf{x}) \frac{\partial \mathbf{C}_\mathbf{y}(\mathbf{x})}{\partial x_l}\right) + 2 \operatorname{Re}\left(\frac{\partial \mathbf{u}^{\mathrm{H}}(\mathbf{x})}{\partial x_k} \mathbf{C}_\mathbf{y}^{-1}(\mathbf{x}) \frac{\partial \mathbf{u}^{\mathrm{H}}(\mathbf{x})}{\partial x_l}\right), \tag{11}$$

$k, l = 1, \ldots, L$.

Now let us consider the DefoSAR data model

$$\tilde{g}_n = \tilde{\gamma} \exp(-j2\pi\tilde{\xi}_n s) \exp(-j(4\pi/\lambda)\psi_n c) + \tilde{\epsilon}_n,$$

$n = 1, \ldots, 2N-2$, where $\tilde{\epsilon}_n$ is complex white Gaussian noise with variance $\sigma_{\tilde{\epsilon}}^2$, and $\psi_n \coloneqq \psi(t_n)$. Here we assume that the elevation estimate is perfect, i.e., $\hat{s} = s$. By replacing $\tilde{\gamma}$ by $a \exp(j\phi)$ where $a, \phi \in \mathbb{R}$, we define the new real parameter vector as $\mathbf{x} \coloneqq \begin{pmatrix} a & c & \phi \end{pmatrix}^{\mathrm{T}}$. The signal vector is given by $u_n(\mathbf{x}) \coloneqq a \exp\big(j(\phi - 2\pi\tilde{\xi}_n s - (4\pi/\lambda)\psi_n c)\big)$, $n = 1, \ldots, 2N-2$. Straightforward computations using (11) yield the Fisher information matrix

$$\mathbf{I}(\mathbf{x}) = \frac{2}{\sigma_{\tilde{\epsilon}}^2} \begin{pmatrix} 2N-2 & 0 & 0 \\ 0 & \frac{(4\pi)^2 a^2}{\lambda^2} \sum_n \psi_n^2 & -\frac{4\pi a^2}{\lambda} \sum_n \psi_n \\ 0 & -\frac{4\pi a^2}{\lambda} \sum_n \psi_n & (2N-2)\gamma^2 \end{pmatrix}.$$

The CRLB for $\hat{c}$ is found to be

$$\sigma_{\hat{c}}^2 \coloneqq [\mathbf{I}^{-1}(\mathbf{x})]_{22} = \frac{\lambda^2 \sigma_{\tilde{\epsilon}}^2}{(4\pi)^2 (2N-2) 2a^2 \sigma_\psi^2}.$$

By defining $SNR \coloneqq a^2/\sigma_{\tilde{\epsilon}}^2$, this reduces to

$$\sigma_{\hat{c}} = \frac{\lambda}{4\pi\sqrt{2N-2}\sqrt{2SNR}\,\sigma_\psi},$$

which completes the proof.

ACKNOWLEDGMENT

TerraSAR-X data was provided by the German Aerospace Center (DLR) under the TanDEM-X Science Phase AO Project NTI_INSA6729. F. Rodriguez Gonzalez assisted on InSAR processing at different stages of the project and discussed with the first author about the pros and cons of the proposed framework. A. Parizzi lectured the first author about Tandem-L and L-band SAR interferometry. H. Breit offered fresh insights into future SAR missions. The original idea of deformation model order selection came out of a discussion with Dr. Y. Wang. The authors would also like to thank Prof. R. Bamler for valuable discussions and the reviewers for their constructive comments.

REFERENCES

[1] A. Moreira, G. Krieger, I. Hajnsek, K. Papathanassiou, M. Younis, P. Lopez-Dekker, S. Huber, M. Villano, M. Pardini, M. Eineder *et al.*, "Tandem-L: A highly innovative bistatic SAR mission for global observation of dynamic processes on the earth's surface," *IEEE Geoscience and Remote Sensing Magazine*, vol. 3, no. 2, pp. 8–23, 2015.

[2] G. Krieger, A. Moreira, H. Fiedler, I. Hajnsek, M. Werner, M. Younis, and M. Zink, "TanDEM-X: A satellite formation for high-resolution SAR interferometry," *IEEE Transactions on Geoscience and Remote Sensing*, vol. 45, no. 11, pp. 3317–3341, 2007.

[3] P. Rizzoli, M. Martone, C. Gonzalez, C. Wecklich, D. B. Tridon, B. Bräutigam, M. Bachmann, D. Schulze, T. Fritz, M. Huber *et al.*, "Generation and performance assessment of the global TanDEM-X digital elevation model," *ISPRS Journal of Photogrammetry and Remote Sensing*, vol. 132, pp. 119–139, 2017.

[4] N. Gebert, B. C. Dominguez, M. W. Davidson, M. D. Martin, and P. Silvestrin, "SAOCOM-CS – a passive companion to SAOCOM for single-pass L-band SAR interferometry," in *EUSAR 2014; 10th European Conference on Synthetic Aperture Radar; Proceedings of*. VDE, 2014, pp. 1–4.

[5] P. López-Dekker, H. Rot, S. Solberg, M. Zonno, M. Rodriguez-Cassola, P. Prats-Iraola, and A. Moreira, "Companion SAR constellations for single-pass interferometric applications: The SESAME mission," in *Geoscience and Remote Sensing Symposium (IGARSS), 2017 IEEE International*. IEEE, 2017, pp. 119–122.

[6] D. Giudici, D. Mapelli, and F. Rocca, "Exploring the potential of Sentinel-1 constellation in tandem and bi-static configurations," in *EUSAR 2018; 12th European Conference on Synthetic Aperture Radar*. VDE, 2018, pp. 1–6.

[7] M. Bartusch, "HRWS high resolution wide swath: the next national X-band SAR mission," in *TerraSAR-X/TanDEM-X Science Team Meeting*, 2016.

[8] J. Janoth, M. Jochum, and A. Kaptein, "The high resolution wide swath mission and WorldSAR," in *37th International Symposium on Remote Sensing of Environment (ISRSE-37)*, 2017.

[9] G. Krieger, M. Zonno, M. Rodriguez Cassola, P. Lopez Dekker, J. Mittermayer, M. Younis, S. Huber, M. Villano, F. Queiroz de Almeida, P. Prats *et al.*, "MirrorSAR: A fractionated space radar for bistatic, multistatic and high-resolution wide-swath SAR imaging," in *International Geoscience and Remote Sensing Symposium (IGARSS)*. IEEE, 2017.

[10] G. Krieger, M. Zonno, J. Mittermayer, A. Moreira, S. Huber, and M. Rodriguez-Cassola, "MirrorSAR: A fractionated space transponder concept for the implementation of low-cost multistatic SAR missions," in *EUSAR 2018; 12th European Conference on Synthetic Aperture Radar*. VDE, 2018, pp. 1–6.

[11] M. Zonno, G. Krieger, M. Rodriguez-Cassola, J. Mittermayer, and A. Moreira, "A MirrorSAR-based single-pass dual-baseline SAR interferometer for the generation of very high quality DEMs," in *EUSAR 2018; 12th European Conference on Synthetic Aperture Radar*. VDE, 2018, pp. 1–6.

[12] H. Ansari, K. Goel, A. Parizzi, F. De Zan, N. Adam, and M. Eineder, "Tandem-L performance analysis for three dimensional earth deformation monitoring," in *Geoscience and Remote Sensing Symposium (IGARSS), 2015 IEEE International*. IEEE, 2015, pp. 4053–4056.

[13] G. Krieger, A. Moreira, M. Zink, I. Hajnsek, S. Huber, M. Villano, K. Papathanassiou, M. Younis, P. L. Dekker, M. Pardini *et al.*, "Tandem-L: Main results of the Phase A feasibility study," in *Geoscience and Remote Sensing Symposium (IGARSS), 2016 IEEE International*. IEEE, 2016, pp. 2116–2119.

[14] P. Prats-Iraola, P. Lopez-Dekker, F. De Zan, N. Yagüe-Martínez, M. Zonno, and M. Rodriguez-Cassola, "Performance of 3-d surface deformation estimation for simultaneous squinted SAR acquisitions," *IEEE Transactions on Geoscience and Remote Sensing*, vol. 56, no. 4, pp. 2147–2158, 2018.

[15] S. Suchandt, A. Pleskachevsky, and D. B. Tridon, "Oceanographic data retrieval with Tandem-L," in *EUSAR 2018; 12th European Conference on Synthetic Aperture Radar*. VDE, 2018, pp. 1–4.

[16] M. Zonno, M. J. Sanjuan-Ferrer, M. Rodriguez-Cassola, G. Krieger, and A. Moreira, "The Tandem-L mission for monitoring of earth's dynamics: Main performance results during Phase-B1," in *EUSAR 2018; 12th European Conference on Synthetic Aperture Radar*. VDE, 2018, pp. 1–6.

[17] A. Reigber and A. Moreira, "First demonstration of airborne SAR tomography using multibaseline L-band data," *IEEE Transactions on Geoscience and Remote Sensing*, vol. 38, no. 5, pp. 2142–2152, 2000.

[18] F. Gini, F. Lombardini, and M. Montanari, "Layover solution in multibaseline SAR interferometry," *IEEE Transactions on Aerospace and Electronic Systems*, vol. 38, no. 4, pp. 1344–1356, 2002.

[19] G. Fornaro, F. Lombardini, and F. Serafino, "Three-dimensional multipass SAR focusing: Experiments with long-term spaceborne data," *IEEE Transactions on Geoscience and Remote Sensing*, vol. 43, no. 4, pp. 702–714, 2005.

[20] F. Lombardini, "Differential tomography: A new framework for SAR interferometry," *IEEE Transactions on Geoscience and Remote Sensing*, vol. 43, no. 1, pp. 37–44, 2005.

[21] G. Fornaro, D. Reale, and F. Serafino, "Four-dimensional SAR imaging for height estimation and monitoring of single and double scatterers," *IEEE Transactions on Geoscience and Remote Sensing*, vol. 47, no. 1, pp. 224–237, 2009.

[22] X. X. Zhu and R. Bamler, "Very high resolution spaceborne SAR tomography in urban environment," *IEEE Transactions on Geoscience and Remote Sensing*, vol. 48, no. 12, pp. 4296–4308, 2010.

[23] ——, "Superresolving SAR tomography for multidimensional imaging of urban areas: Compressive sensing-based TomoSAR inversion," *IEEE Signal Processing Magazine*, vol. 31, no. 4, pp. 51–58, 2014.

[24] I. Hajnsek, T. Busche, G. Krieger, M. Zink, and A. Moreira, "Announcement of opportunity: TanDEM-X science phase," *DLR Public Document TD-PD-PL-0032*, no. 10, 2014.

[25] A. Ferretti, A. Fumagalli, F. Novali, C. Prati, F. Rocca, and A. Rucci, "A new algorithm for processing interferometric data-stacks: SqueeSAR," *IEEE Transactions on Geoscience and Remote Sensing*, vol. 49, no. 9, pp. 3460–3470, 2011.

[26] A. Parizzi and R. Brcic, "Adaptive InSAR stack multilooking exploiting amplitude statistics: A comparison between different techniques and practical results," *IEEE Geoscience and Remote Sensing Letters*, vol. 8, no. 3, pp. 441–445, 2011.

[27] M. Schmitt and U. Stilla, "Adaptive multilooking of airborne single-pass multi-baseline InSAR stacks," *IEEE Transactions on Geoscience and Remote Sensing*, vol. 52, no. 1, pp. 305–312, 2014.

[28] X. X. Zhu and R. Bamler, "Super-resolution power and robustness of compressive sensing for spectral estimation with application to spaceborne tomographic SAR," *IEEE Transactions on Geoscience and Remote Sensing*, vol. 50, no. 1, pp. 247–258, 2012.

[29] R. Bamler, M. Eineder, N. Adam, X. Zhu, and S. Gernhardt, "Interferometric potential of high resolution spaceborne SAR," *Photogrammetrie-Fernerkundung-Geoinformation*, vol. 2009, no. 5, pp. 407–419, 2009.

[30] X. X. Zhu and R. Bamler, "Tomographic SAR inversion by L_1-norm regularization–the compressive sensing approach," *IEEE Transactions on Geoscience and Remote Sensing*, vol. 48, no. 10, pp. 3839–3846, 2010.

[31] A. Budillon, A. Evangelista, and G. Schirinzi, "Three-dimensional SAR focusing from multipass signals using compressive sampling," *IEEE Transactions on Geoscience and Remote Sensing*, vol. 49, no. 1, pp. 488–499, 2011.

[32] K. Goel and N. Adam, "Fusion of monostatic/bistatic InSAR stacks for urban area analysis via distributed scatterers," *IEEE Geoscience and Remote Sensing Letters*, vol. 11, no. 4, pp. 733–737, 2014.

[33] S. Boyd, N. Parikh, E. Chu, B. Peleato, J. Eckstein *et al.*, "Distributed optimization and statistical learning via the alternating direction method of multipliers," *Foundations and Trends® in Machine learning*, vol. 3, no. 1, pp. 1–122, 2011.

[34] X. Zhu and R. Bamler, "Demonstration of super-resolution for tomographic SAR imaging in urban environment." *IEEE Trans. Geoscience and Remote Sensing*, vol. 50, no. 8, pp. 3150–3157, 2012.

[35] M. Nannini, M. Martone, P. Rizzoli, P. Prats-Iraola, M. Rodriguez-Cassola, and A. Moreira, "Spaceborne demonstration of coherent SAR

tomography for future companion satellite SAR missions," in *Geoscience and Remote Sensing Symposium (IGARSS), 2017 IEEE International*. IEEE, 2017, pp. 129–132.

[36] F. Kugler, D. Schulze, I. Hajnsek, H. Pretzsch, and K. P. Papathanassiou, "TanDEM-X Pol-InSAR performance for forest height estimation," *IEEE Transactions on Geoscience and Remote Sensing*, vol. 52, no. 10, pp. 6404–6422, 2014.

[37] A. Ferretti, C. Prati, and F. Rocca, "Permanent scatterers in SAR interferometry," *IEEE Transactions on geoscience and remote sensing*, vol. 39, no. 1, pp. 8–20, 2001.

[38] C. Colesanti, A. Ferretti, F. Novali, C. Prati, and F. Rocca, "SAR monitoring of progressive and seasonal ground deformation using the permanent scatterers technique," *IEEE Transactions on Geoscience and Remote Sensing*, vol. 41, no. 7, pp. 1685–1701, 2003.

[39] N. Adam, B. Kampes, and M. Eineder, "Development of a scientific permanent scatterer system: Modifications for mixed ERS/ENVISAT time series," in *Envisat & ERS Symposium*, vol. 572, 2005.

[40] N. Ge, F. R. Gonzalez, Y. Wang, Y. Shi, and X. X. Zhu, "Spaceborne staring spotlight SAR tomographya first demonstration with TerraSAR-X," *IEEE Journal of Selected Topics in Applied Earth Observations and Remote Sensing*, no. 99, pp. 1–14, 2018.

[41] X. X. Zhu, N. Ge, and M. Shahzad, "Joint sparsity in SAR tomography for urban mapping," *IEEE Journal of Selected Topics in Signal Processing*, vol. 9, no. 8, pp. 1498–1509, 2015.

[42] G. Fornaro, S. Verde, D. Reale, and A. Pauciullo, "CAESAR: An approach based on covariance matrix decomposition to improve multibaseline–multitemporal interferometric sar processing," *IEEE Transactions on Geoscience and Remote Sensing*, vol. 53, no. 4, pp. 2050–2065, 2015.

[43] M. Schmitt and U. Stilla, "Compressive sensing based layover separation in airborne single-pass multi-baseline InSAR data," *IEEE Geoscience and Remote Sensing Letters*, vol. 10, no. 2, pp. 313–317, 2013.

[44] X. X. Zhu and M. Shahzad, "Facade reconstruction using multiview spaceborne TomoSAR point clouds," *IEEE Transactions on Geoscience and Remote Sensing*, vol. 52, no. 6, pp. 3541–3552, 2014.

[45] A. Parizzi, X. Cong, and M. Eineder, "First results from multifrequency interferometry. a comparison of different decorrelation time constants at L, C, and X band," *ESA Scientific Publications*, no. SP-677, pp. 1–5, 2009.

[46] Y. Morishita and R. F. Hanssen, "Temporal decorrelation in L-, C-, and X-band satellite radar interferometry for pasture on drained peat soils," *IEEE Transactions on Geoscience and Remote Sensing*, vol. 53, no. 2, pp. 1096–1104, 2015.

[47] S. Gernhardt and R. Bamler, "Deformation monitoring of single buildings using meter-resolution SAR data in PSI," *ISPRS journal of photogrammetry and remote sensing*, vol. 73, pp. 68–79, 2012.

[48] S. Auer, I. Hornig, M. Schmitt, and P. Reinartz, "Simulation-based interpretation and alignment of high-resolution optical and SAR images," *IEEE Journal of Selected Topics in Applied Earth Observations and Remote Sensing*, vol. 10, no. 11, pp. 4779–4793, 2017.

[49] Y. Sun, M. Shahzad, and X. X. Zhu, "Building height estimation in single SAR image using OSM building footprints," in *Urban Remote Sensing Event (JURSE), 2017 Joint*. IEEE, 2017, pp. 1–4.

[50] S. M. Kay, *Fundamentals of statistical signal processing: estimation theory*. Prentice Hall, 1993, vol. 1.

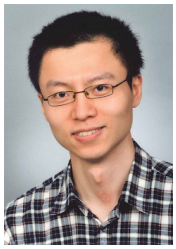

Nan Ge received the bachelor and master degrees in Geoenvironmental Engineering from TU Clausthal, Germany. Since 2013, he has been pursuing his doctoral degree by developing advanced tomographic techniques for very high resolution SAR systems at the Remote Sensing Technology Institute, German Aerospace Center (DLR).

Xiao Xiang Zhu (S'10–M'12–SM'14) received the Master (M.Sc.) degree, her doctor of engineering (Dr.-Ing.) degree and her Habilitation in the field of signal processing from Technical University of Munich (TUM), Munich, Germany, in 2008, 2011 and 2013, respectively.

She is currently the Professor for Signal Processing in Earth Observation (www.sipeo.bgu.tum.de) at Technical University of Munich (TUM) and German Aerospace Center (DLR); the head of the department "EO Data Science" at DLR's Earth Observation Center; and the head of the Helmholtz Young Investigator Group "SiPEO" at DLR and TUM. Prof. Zhu was a guest scientist or visiting professor at the Italian National Research Council (CNR-IREA), Naples, Italy, Fudan University, Shanghai, China, the University of Tokyo, Tokyo, Japan and University of California, Los Angeles, United States in 2009, 2014, 2015 and 2016, respectively. Her main research interests are remote sensing and Earth observation, signal processing, machine learning and data science, with a special application focus on global urban mapping.

Dr. Zhu is a member of young academy (Junge Akademie/Junges Kolleg) at the Berlin-Brandenburg Academy of Sciences and Humanities and the German National Academy of Sciences Leopoldina and the Bavarian Academy of Sciences and Humanities. She is an associate Editor of IEEE Transactions on Geoscience and Remote Sensing.